Petroleum Science 20 (2023) 2268–2281

Contents lists available at ScienceDirect

Petroleum Science

journal homepage: www.keaipublishing.com/en/journals/petroleum-science

Original Paper

Efficient production optimization for naturally fractured reservoir using EDFM

Jian-Chun Xu [a, b, *], Wen-Xin Zhou [a, b], Hang-Yu Li [a, b]

[a] Key Laboratory of Unconventional Oil & Gas Development, China University of Petroleum (East China), Ministry of Education, Qingdao, 266580, Shandong, PR China
[b] School of Petroleum Engineering, China University of Petroleum (East China), Qingdao, 266580, Shandong, PR China

ARTICLE INFO

Article history:
Received 16 September 2022
Received in revised form
12 February 2023
Accepted 13 February 2023
Available online 14 February 2023

Edited by Yan-Hua Sun

Keywords:
Production optimization
Naturally fractured reservoir
Embedded discrete fracture method
StoSAG algorithm
PSO algorithm

ABSTRACT

Naturally fractured reservoirs make important contributions to global oil and gas reserves and production. The modeling and simulation of naturally fractured reservoirs are different from conventional reservoirs as the existence of natural fractures. To address the development optimization problem of naturally fractured reservoirs, we propose an optimization workflow by coupling the optimization methods with the embedded discrete fracture model (EDFM). Firstly, the effective and superior performance of the workflow is verified based on the conceptual model. The stochastic simplex approximate gradient (StoSAG) algorithm, the ensemble optimization (EnOpt) algorithm, and the particle swarm optimization (PSO) algorithm are implemented for the production optimization of naturally fractured reservoirs based on the improved versions of the Egg model and the PUNQ-S3 model. The results of the two cases demonstrate the effectiveness of this optimization workflow by finding the optimal well controls which yield the maximum net present value (NPV). Compared to the initial well control guess, the final NPV obtained from the production optimization of fractured reservoirs based on all three optimization algorithms is significantly enhanced. Compared with the optimization results of the PSO algorithm, StoSAG and EnOpt have significant advantages in terms of final NPV and computational efficiency. The results also show that fractures have a significant impact on reservoir production. The economic efficiency of fractured reservoir development can be significantly improved by the optimization workflow.

1. Introduction

Reservoir development dynamics are influenced by various factors such as geological conditions and production working conditions. To improve the economic efficiency of reservoir development, relevant production decision variables need to be adjusted timely according to reservoir dynamics (Yang et al., 2017; Wang et al., 2016). Decision variables that satisfy the constraints tend to form many combinations of potential optimal solutions. Therefore, it is difficult to rely solely on the engineers' intuition to determine the optimal solution (Al Dossary and Nasrabadi, 2016). Currently, commonly used methods for reservoir development optimization are combining reservoir numerical simulation techniques with various optimization algorithms. Reservoir numerical simulation techniques are used to simulate the production dynamics of reservoirs under different operating conditions and provide the required production data for subsequent optimization algorithms. Optimization algorithms then search for the optimal solution based on this data to obtain the best development plan (Chen et al., 2020). Therefore, accurate and effective reservoir modeling methods and efficient optimization algorithms are necessary for reservoir production optimization.

Almost all reservoirs have developed natural fractures to some extent (Olorode et al., 2020). Fractures have a significant impact on the flow behavior of reservoir fluids. For example, during the implementation of enhanced oil recovery (EOR), the effectiveness of EOR can be significantly reduced due to the channeling of injected fluids through fractures. In turn, for shale reservoirs, fractures from hydraulic fracturing are necessary for the flow of

* Corresponding author. Key Laboratory of Unconventional Oil & Gas Development, China University of Petroleum (East China), Ministry of Education, Qingdao, 266580, Shandong, PR China.
E-mail address: 20170048@upc.edu.cn (J.-C. Xu).

https://doi.org/10.1016/j.petsci.2023.02.007

shale oil and gas in them. This makes the economic production of shale reservoirs possible. In addition, these fractures facilitate the initial production increase of shale reservoirs. Therefore, techniques are needed for fractured reservoirs to characterize the flow in such reservoirs (Soleimani, 2017). Characterization of fractures in reservoirs is a challenging problem due to the extreme non-homogeneity and anisotropy of fractures (Torcuk et al., 2013). A large amount of work has been done by researchers to develop accurate numerical simulation models to characterize the seepage of reservoir fractures.

Warren and Root (1963) were among the first to use a dual-porosity model (DPM) to study naturally fractured reservoir flow. Because of the large limitations of the DPM method, the discrete fracture model (DFM) for characterizing fractured reservoirs was proposed by Karimi-Fard and Firoozabadi (2003). To avoid the extensive unstructured mesh dissection process required for DFM models to deal with complex fractures, Li and Lee (2008) proposed the EDFM. The simulation of fractures in reservoirs using the EDFM method has received increasing attention from researchers because of the advantages of EDFM as strong fracture network characterization and low simulation cost (Sun and Xu, 2022). Chai et al. (2018a) developed a modeling approach for fractured shale reservoirs combining EDFM and multiple porosity/permeability method. The improved model decreases the complexity of the gridding process and improves the accuracy of fluid transport within and between different porosity types. Xu et al. (2018) used EDFM to simulate reservoirs in the Mancos Shale of the Piceance Basin and showed that the EDFM method can be successfully applied to model shale reservoirs at the field scale. Chai et al. (2018b) developed a compartmental EDFM (cEDFM) based on the original EDFM. Unlike the original method, the fractures split the matrix grid blocks in cEDFM. This model was then benchmarked and its accuracy was evaluated by comparison with fine explicit cases. The results show that the improved model yields better accuracy even for multiphase flow simulations with flow barriers. The model was then applied to history matching and uncertainties were quantified for the fracture network for two synthetic cases. Fiallos et al. (2019) studied the effect of inter-well interference based on EDFM and history matching. Based on the actual production data, they established a model that can be successfully applied to oil fields. Chang et al. (2020) proposed a well-spacing optimization method based on EDFM and applied it to actual shale gas reservoirs. The effects of reservoir uncertainty and fracture parameters are considered in the study. Jia and Xian (2022) applied 3D EDFM to simulate the process of pulse-decay experiments in fractured shale cores. Zhu et al. (2020) developed an EDFM on the basis of the corner grid and coupled it with local grid refinement. Parameter optimization of a multi-stage fractured horizontal well was implemented. Torres et al. (2021) optimized the numerical simulation of reservoirs with complex fracture systems and refined previous comprehensive description techniques for Eagle Ford shale oil based on the EDFM.

However, the experimental results of Țene et al. (2017) showed that the EDFM model is not suitable in the case where the fracture permeability is lower than the matrix permeability. In addition, the existing EDFM formulation ignores the properties of the fracture between adjacent matrix cells. To address the limitations of the above methods, they proposed projection-based EDFM (pEDFM), and the results showed that pEDFM significantly outperformed the original EDFM. Researchers then carried out a lot of work around this new method. Rao et al. (2020) pointed out the limitations such as the lack of practical projection surface selection methods and the poor performance in some cases in the original pEDFM. The corresponding modification methods are proposed to address these limitations. Then the necessity and effectiveness of these modified methods are illustrated by some test cases. Finally, the robustness of the modified pEDFM for practical applications in fractured reservoirs is illustrated by examples. Liu et al. (2020) implemented the pEDFM method to evaluate the CO_2 sequestration capacity of shale gas reservoirs with complex boundary shapes. The method was also compared with the commercial software CMG to verify the validity of the method. Finally, a field case in the New Albany Shale was used to illustrate the practical application of the proposed model in simulating the CO_2 sequestration process and evaluating the CO_2 sequestration capacity. Rao et al. (2022) applied the pEDFM method to the numerical simulation of two-phase heat and mass transfer in fractured reservoirs. The numerical simulation results showed that the accuracy of temperature and saturation distribution calculated using pEDFM is much higher than that of EDFM when the multiphase flow crosses the fractures or there are flow barriers in the reservoir. The results of the study indicate that pEDFM can be more accurately and effectively applied to the numerical simulation in realistic fractured reservoirs under complex geological conditions.

In terms of optimization algorithms, researchers have tried to introduce various algorithms into the field of reservoir production optimization in recent years (Chen and Reynolds, 2018; Feng et al., 2022; Wu et al., 2022; Xue et al., 2021). Depending on whether the optimization process involves the computation of gradients, these algorithms can be categorized as derivative-free and gradient-based optimization algorithms. Gradient-based methods are computationally efficient, but the true gradient is always difficult to obtain (Zhang et al., 2014). The advantages of the derivative-free optimization algorithm are mainly the high global optimization capability and robustness, and it also allows dealing with non-differentiable variables, etc. These algorithms include genetic algorithms (GA) (Murray et al., 2020), PSO (Lee and Stephen, 2019; Jia et al., 2020), simulated annealing algorithms (Tukur et al., 2019), long short-term memory (LSTM) algorithms (Zhu et al., 2022; Pan et al., 2022), etc. Ma et al. (2022) implemented well-control optimization for the 3D Bruges case model based on the PSO algorithm and the multi-group optimization strategy they developed. Nasir et al. (2022) used a two-stage optimization strategy based on the PSO-mesh adaptive direct search (MADS) algorithm for solving the large-scale oil field well location optimization problem. The derivative-free optimization methods have the above-mentioned advantages. However, they all require a large number of reservoir simulation runs to ensure global search capability. Therefore, the computational cost is relatively high. Considering the advantages of gradient-based algorithms and the difficulties in obtaining real gradients, researchers introduced the approximate gradient method. One of the approximate gradient methods is EnOpt, as first proposed by Lorentzen et al. (2006) and Nwaozo (2006). With the progress of research on the EnOpt, Fonseca et al. (2017) proposed the StoSAG, which is an improved version of EnOpt with better performance in robust optimization. Subsequently, researchers have carried out much research work around StoSAG. Chen et al. (2017) used StoSAG based on the lexicographic method framework to achieve robust production optimization with the minimization of associated risks or uncertainties. The effectiveness of the framework was also validated in two reservoir examples. Lu et al. (2017) proposed an adaptive robust optimization algorithm based on the StoSAG. The method utilizes the method of selecting a subset of realizations to reduce the number of realizations involved in robust optimization while preserving the characteristics of the set of realizations. The optimization results of all three cases show that the algorithm effectively improves the convergence speed and also finds a higher optimal NPV. Liu and Forouzanfar (2018) combined a hierarchical clustering approach and StoSAG to achieve robust optimization of well control in naturally fractured reservoirs by

selecting representative models. Chen and Xu (2019) provide a theoretical discussion on the phenomenon of StoSAG superiority over EnOpt and a comparative validation on the Brugge field case.

In this work, our objective is to couple the optimization algorithm (StoSAG, EnOpt, and PSO) with EDFM to form a fractured reservoir optimization workflow and to investigate the performance of the workflow. We first introduce three kinds of optimization algorithm and couple the EDFM with them. Then, the grid refinement method is used to verify the effectiveness of the workflow for fractured reservoir production optimization. Finally, two case studies based on actual reservoir models demonstrate the applicability of the workflow in fractured reservoir production optimization.

2. Optimization algorithm

In reservoir development optimization, it is common to use the NPV or cumulative oil production, etc., as the objective function. In the work of this paper, we choose the NPV over the production life of fractured reservoirs as the objective function, with the well control variables as optimization variables, other settings kept constant, and all drilling costs ignored.

The formula for calculating NPV is as follows.

$$J(\mathrm{m}_i,u)=\sum_{n=1}^{N_t}\left\{\frac{\Delta t_n}{(1+b)^{\frac{t_n}{365}}}\left[\sum_{j=1}^{N_W}\left(r_o\cdot\overline{q_{o,j}^n}+r_g\cdot\overline{q_{g,j}^n}-c_w\overline{q_{w,j}^n}\right)-\sum_{k=1}^{N_I}\left(c_{wi}\cdot\overline{q_{wi,k}^n}\right)\right]\right\} \tag{1}$$

where u is a N_u-dimensional well control vector; n is the n^{th} time step for the reservoir production; N_t is the total number of time steps; t_n is the time at the end of the n^{th} time step; Δt_n is the n^{th} time step size; b is the annual discount rate; N_W and N_I are the number of production wells and injection wells, respectively; r_o is the oil revenue, \$/m^3; r_g is the price of natural gas, \$/m^3; c_w and c_{wi} denote the disposal cost of produced water and the cost of water injection, respectively, \$/m^3; $q_{o,j}^n$ and $q_{w,j}^n$, respectively, denote the average oil production rate and the average water production rate of j^{th} production well during the n^{th} time step, m^3/day; $q_{g,j}^n$ is the average gas production rate of j^{th} production well during the n^{th} time step, m^3/day; $q_{wi,k}^n$ denote the average water injection rate of k^{th} injection well during the n^{th} time step, m^3/day.

2.1. StoSAG

In this paper, logarithmic transformation is introduced in the StoSAG implementation referring to the article by Chen and Xu (2019). Firstly, the optimized variable x in the domain $[x^{\mathrm{low}}, x^{\mathrm{up}}]$ is converted to the variable u in the domain $[-\infty,\infty]$ for the optimization search according to Eq. (2), and then u is converted back to the actual well-control vector x and run the simulation according to Eq. (3).

$$u_i=\ln\left(\frac{x_i-x_i^{\mathrm{low}}}{x_i^{\mathrm{up}}-x_i}\right) \tag{2}$$

$$x_i=\frac{\exp(u_i)\cdot x_i^{\mathrm{up}}+x_i^{\mathrm{low}}}{1+\exp(u_i)} \tag{3}$$

For a general optimization problem, the formula for the search direction of StoSAG is given in Eq. (4).

$$d_l=\nabla_u J(u,\mathrm{m}) \tag{4}$$

where u is the log-transformed well-control vector; m denotes the realization for reservoir model; $\nabla_u J(u,\mathrm{m})$ is the stochastic approximation of the gradient, which is obtained by Eq. (5).

$$\nabla_u J(u,\mathrm{m})=\frac{1}{N_p}\sum_{j=1}^{N_p}\left(\delta\hat{u}_{l,j}\left(\delta\hat{u}_{l,j}\right)^T\right)^{+}\delta\hat{u}_{l,j}\left(J\left(\hat{u}_{l,j},\mathrm{m}\right)-J(u_l,\mathrm{m})\right) \tag{5}$$

where N_p is the number of control perturbations, and each control perturbation $\hat{u}_{l,j},\ j=1,2,\ldots,N_p$, is generated from the distribution $N(u_l,\boldsymbol{C}_U)$ at iteration l; $\boldsymbol{C}_U$ is a predefined covariance matrix which is defined as shown in Eq. (6). The superscript sign "+" denotes the Moore-Penrose pseudo-inverse, and $\delta\hat{u}_{l,j}=\hat{u}_{l,j}-\hat{u}_l$.

$$\boldsymbol{C}_U=\begin{pmatrix}C_U^1 & 0 & \cdots & 0\\ 0 & C_U^2 & \cdots & 0\\ \vdots & \vdots & \vdots & \vdots\\ 0 & 0 & \cdots & C_U^w\end{pmatrix} \tag{6}$$

where $\boldsymbol{C}_U^w, w=1,2,\ldots,n_{\mathrm{well}}$ is a covariance matrix; n_{well} is the total number of well (Chen and Xu, 2019).

2.2. EnOpt

The basic search direction of the EnOpt algorithm is expressed as:

$$d_{k,\mathrm{EnOpt}}=\frac{1}{N_p-1}\sum_{i=1}^{N_p}\left(\hat{u}_{k,i}-\overline{\hat{u}_k}\right)\left(J\left(\mathrm{m},\hat{u}_{k,i}\right)-\overline{J(\mathrm{m},u_k)}\right) \tag{7}$$

with

$$\overline{\hat{u}_k}=\frac{1}{N_p}\sum_{i=1}^{N_p}\hat{u}_{k,i},\overline{J(\mathrm{m},u_k)}=\frac{1}{N_p}\sum_{i=1}^{N_p}J(\mathrm{m},\hat{u}_{k,i}) \tag{8}$$

where control perturbation $\hat{u}_{k,i},\ i=1,2,3,\ldots,N_p$, is generated by the distribution $\mathcal{N}(u_k,\boldsymbol{C}_U)$ at the k^{th} iteration. After obtaining the approximate gradient, the steepest ascent method is used to find the optimum. The convergence condition of the EnOpt algorithm is the same as that of the StoSAG algorithm.

2.3. PSO

The third algorithm used in this paper, the PSO algorithm, is a typical derivative-free algorithm (Han et al., 2021). The particle swarm is first initialized randomly in the solution space. Then each particle updates its position and velocity by tracking the individual extremum and the global extremum. Where the individual extremum is the optimal solution found by each particle itself, and the global extremum is the optimal solution found by all particles in the swarm. The algorithm uses the fitness value to evaluate the potential of the current particle to become the target solution. In this paper, the fitness value is the NPV obtained by simulating the corresponding well control vector for each particle.

For an optimization problem where the swarm consists of N particles in a d-dimensional search space, where the velocity and position of each particle are updated by the following equations.

$$\begin{cases} v_{i,d}^{k+1} = \omega v_{i,d}^{k} + c_1 r_1^k \left(p_{i,d}^k - x_{i,d}^k\right) + c_2 r_2^k \left(g_d^k - x_{i,d}^k\right) \\ x_{i,d}^{k+1} = x_{i,d}^k + v_{i,d}^{k+1}, i = 1, 2, ..., N \end{cases} \tag{9}$$

where ω is the inertia weight; v_i^k is the velocity of the i^{th} particle in the k^{th} iteration; c_1 and c_2 are the learning factor; r_1^k and r_2^k are the uniform random number in the range of [0,1] generated in the k^{th} iteration; x_i^k is the position of the i^{th} particle in the k^{th} iteration; p_i^k is the optimal position searched by the i^{th} particle up to now, which is the individual extreme value; g^k is the optimal position searched by the whole particle population up to now, which is the global extreme value.

3. EDFM-based simulation

In the EDFM implementation, the fractured mesh and the matrix mesh are not intersected in the physical domain; instead, they are connected in the computational domain by the non-neighboring connection (NNC). The above approach allows EDFM to balance the structured mesh of the matrix with the simulation of complex fractures (Xu and Sepehrnoori, 2019). Thus, the method can be implemented in a reservoir simulator with NNC capabilities for the simulation of complex fractured reservoirs.

A key point for the EDFM method to be successfully implemented is the calculation of the transmissibility factor in the NNC. Because this point is related to the accuracy of the calculated fluid transfer between the fracture grid and the matrix grid, between different fracture grids of the same fracture, and between fracture grids of different fractures. To calculate the transmissibility factor accurately, we use the calculation formula in the article of Moinfar et al. (2014). Depending on the fracture cells' mass transfer objects, NNCs are classified into the following three types: I. NNCs between the fracture cell and its embedded matrix cell; II. NNCs between different fracture cells in the same fracture; III. NNCs between intersecting fracture cells. The general formula for calculating the transmissibility factor for the three cases is as follows.

$$T = \frac{A^{\text{NNC}} \times k^{\text{NNC}}}{d^{\text{NNC}}} \tag{10}$$

When calculating the transmissibility factor between the fracture cell and its embedded matrix cell, the physical meaning of each symbol in Eq. (10) is as follows. A^{NNC} is the surface area of fractures embedded in the matrix grid block; k^{NNC} is the harmonic average of the matrix permeability and fracture permeability; d^{NNC} refers to the average normal distance, which is calculated as follows Eq. (11) (Li and Lee, 2008; Hajibeygi et al., 2011).

$$d^{\text{NNC}} = \frac{\int_V x_n \mathrm{d}v}{V} \tag{11}$$

where $\mathrm{d}v$ is the volume element; x_n is the normal distance of the element from the fracture; and V is the volume of matrix gridblock.

When calculating the transmissivity of the NNC between two intersecting fracture segments, the method of Karimi-Fard et al. (2004) was applied and its formula is shown in Eqs. (12) and (13) below.

$$\frac{k^{\text{NNC}} A^{\text{NNC}}}{d^{\text{NNC}}} = \frac{T_1 T_2}{T_1 + T_2} \tag{12}$$

$$T_1 = \frac{k_{\text{f1}} \omega_{\text{f1}} L_{\text{int}}}{d_{\text{f1}}}, T_2 = \frac{k_{\text{f2}} \omega_{\text{f2}} L_{\text{int}}}{d_{\text{f2}}} \tag{13}$$

where L_{int} is the length of the intersection lines constrained in a gridblock; ω_{f} and k_{f} are the width and permeability of the fracture, respectively; d_{f} is the average normal distance from the center of the fracture sub-segment (located on both sides of the intersection line) to the intersection line (Moinfar et al., 2014).

When calculating the transmissibility of the NNC between different fracture cells in the same fracture, the physical meaning of each symbol in Eq. (10) is as follows. k^{NNC} is the fracture permeability; d^{NNC} is the distance between the centers of two fracture segments; and A^{NNC} is the area of the adjacent face of two adjacent fracture grids.

4. Production optimization workflow

The main idea of our workflow is to couple a fractured reservoir modeling approach (EDFM) with the optimization algorithms to build a fractured reservoir production optimization system based on both. The ensemble optimization workflow combined with the EDFM method is shown in Fig. 1. In our implementation, we use the NNC approach to achieve the embedding of different forms of fractures. Although we mainly consider vertical, horizontal, and 45° inclined fracture distribution morphologies in our case, the embedding of more complex fracture networks can actually be accomplished by the NNC method. It is important to note that accurate numerical simulation models for fractured reservoirs are the basis for NPV calculations and StoSAG gradient calculations in the optimization process. Therefore, we verify the validity of the EDFM method in the next section.

5. Validation

To verify the validity of the EDFM method using the commercial software, we modeled the same fractured reservoir using the EDFM method and the grid refinement method, respectively, and compared the simulation results of both. We chose cumulative production (oil and water) and daily production (oil and water) as comparative indicators. This is because they are closely related to the calculation of the objective function (NPV) used in production optimization.

5.1. Intersected orthogonal fractures

We use a 2D fractured reservoir model with five intersecting fractures as the validation model in this part, and the geological schematic of the model is shown in Fig. 2. The reservoir model size is 200 m × 100 m × 4 m. The main fracture length is 132 m, the sub-fracture length is 40 m, and the sub-fracture spacing is 44 m. The reservoir contains one injector and one producer. The permeability and porosity of the matrix are 10 mD and 0.1, respectively. The conductivity of all fractures is 100 mD m. The compressibility coefficient for water and rock are 1.2×10^{-5} and 6.103×10^{-5} psi^{-1}, respectively. The initial reservoir formation pressure is 3596.94 psi with a production life of 3000 days.

The grid is divided into 152 × 63 × 1 cells in the grid refinement model. In the horizontal direction, the grid size is gradually changed near the fracture to ensure the simulation accuracy of fluid flow near the fracture. We created a grid refinement area of 8 m around the fracture for each fracture. For the EDFM model, a uniform 100 × 50 × 1 matrix grid and 106 fracture cells were used. Both injection and production wells are controlled by constant pressure, with BHP settings of 3596.94 and 797.71 psi for the

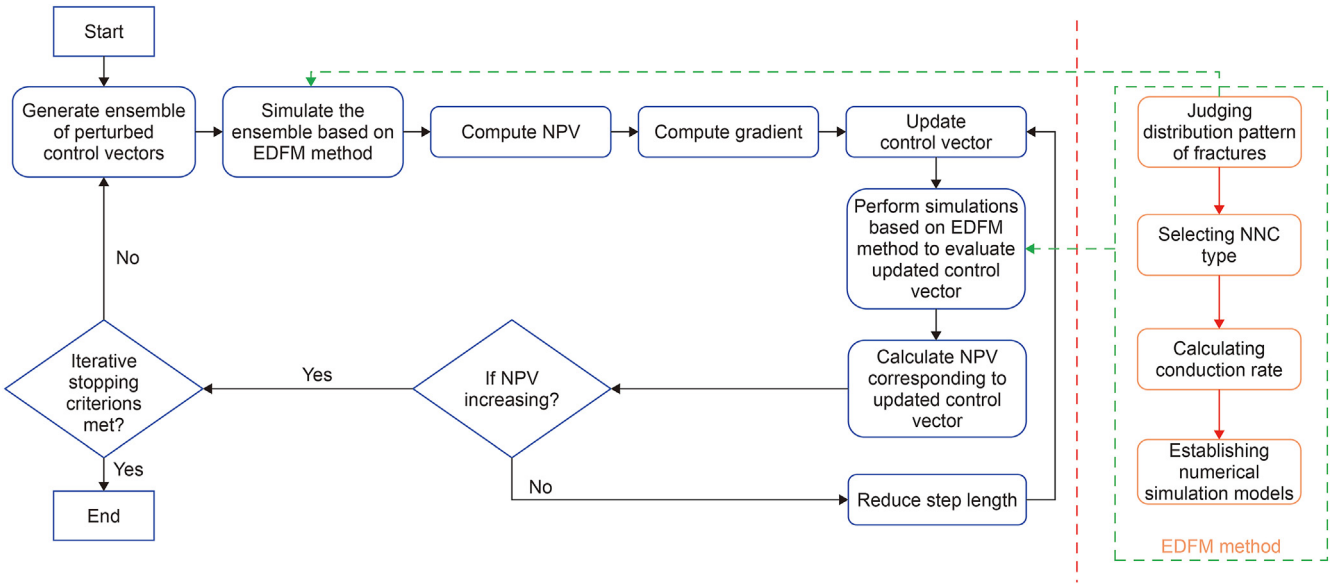

Fig. 1. Production optimization workflow using EDFM.

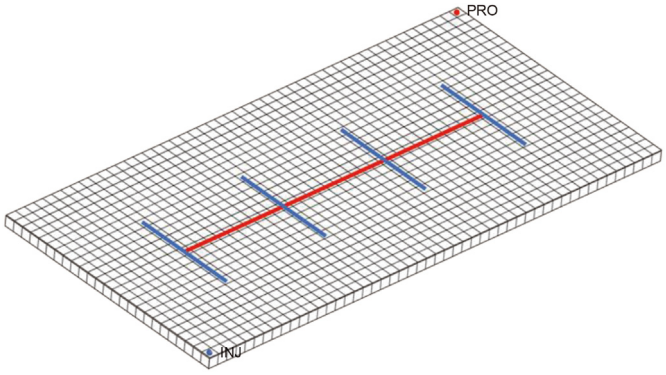

Fig. 2. Schematic of the fractured reservoir with five intersecting fractures.

injection well and production well, respectively.

From the results of each production data given in Fig. 3, the EDFM method used in this paper achieved almost the same results as the fine-grid model in modeling intersected orthogonal fractures, which verifies the effectiveness of the EDFM approach in modeling intersected orthogonal fractures in this paper.

5.2. Dipping fracture

Here we modeled a dipping fracture using EDFM and Cartesian single porosity model respectively and compared their results. The latter uses a stair-stepping representation of the dipping fracture, as shown in Fig. 4.

The size of this reservoir model is 4 m × 4 m × 1 m. The fracture is located in the middle area of the model with a length of $2\sqrt{2}$ m. One injection well and one production well are in one corner of the reservoir model. Both injection and production wells are controlled by constant pressure, with BHP settings of 3596.94 and 797.71 psi for injection and production wells, respectively. The permeability and porosity of the matrix are 1mD and 0.1. The conductivity of the fracture is 1.414 mD m. The compressibility coefficient for water and rock are 1.2×10^{-5} and 6.103×10^{-5} psi^{-1}, respectively. The initial reservoir formation pressure is 3596.94 psi with a production life of 100 days. Note that there is a discrepancy between the fracture grid length in the EDFM method and its actual length embedded in the matrix grid due to the tilted placement of the fracture. The settings of some parameters need to be corrected.

The simulation results of the two modeling methods for the non-orthogonal fracture model shown in Fig. 4 are given in Fig. 5. From the figure, we can see that the EDFM method achieves almost the same results as the Cartesian single porosity model in the simulation of non-orthogonal fractures, which verifies the effectiveness of the EDFM method in modeling non-orthogonal fractures.

6. Examples and results

In this section, we combine the StoSAG algorithm with the EDFM method to form a fractured reservoir optimization method, which is applied in the production optimization of a conceptual model and two fractured reservoirs based on actual reservoir models, respectively. The corresponding optimization results are also compared with those of EnOpt and PSO algorithms to determine the optimization performance of the method. All algorithmic programs were implemented and run by Matlab 2019a, and all simulations were run by the commercial software ECLIPSE. The computing device is a Core i5 computer with a CPU processing frequency of 3 GHz and 16 GB of RAM.

6.1. Example 1: Conceptual model

To further validate the stability of the EDFM method in the production optimization process of fractured reservoirs, we first conducted a production optimization study of a conceptual model. The fractures in the model are all orthogonal, and this setup facilitates us to build the corresponding grid refinement reservoir model. The schematic diagram of the conceptual model and the distribution of fractures are shown in Fig. 6a. The matrix permeability is 10 mD. The porosity of the matrix is 0.1. The conductivity of all fractures is 8.3333×10^4 mD m. The initial reservoir formation pressure is 3596.93 psi with a production life of 3000 days. In the EDFM method, the model consists of 100 × 100 × 1 matrix grids and 440 fracture cells with a matrix grid size of $\Delta x = \Delta y = 2$ m,

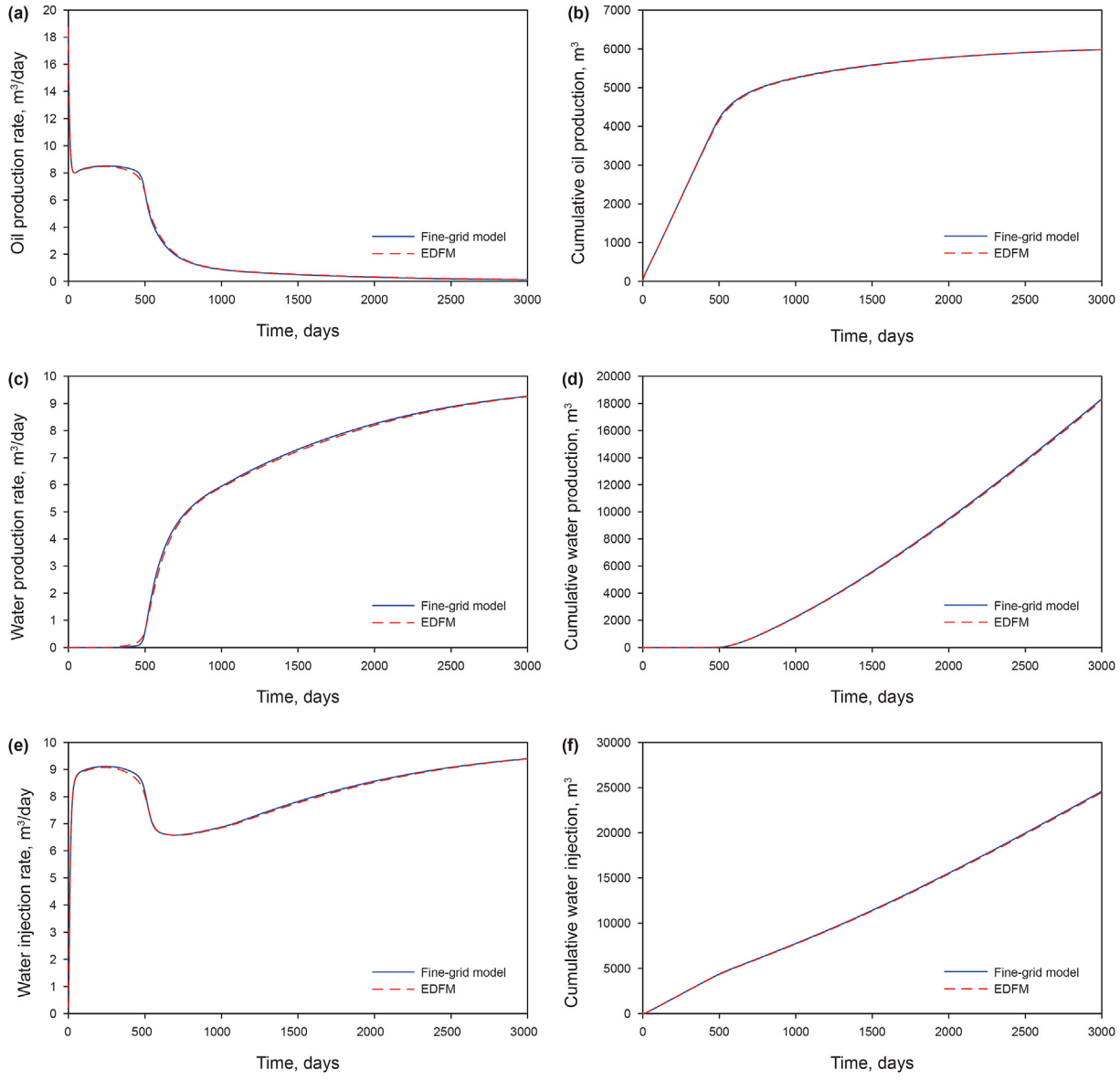

Fig. 3. Comparison of (**a**) oil production rate, (**b**) cumulative oil production, (**c**) water production rate, (**d**) cumulative water production, (**e**) water injection rate, and (**f**) cumulative water injection during 3000 days for the model shown in Fig. 2, modeled by the fine-grid model and EDFM model.

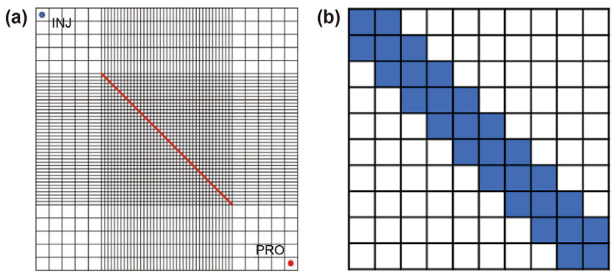

Fig. 4. (**a**) Geometric representation of the fractured reservoir containing an inclined fracture. (**b**) A partial enlargement of the model shown in Fig. 4a.

$\Delta z = 10$ m. In the mesh refinement model, we use local mesh refinement to simulate 16 intersecting small fractures in the reservoir model and global mesh refinement to simulate the other three large fractures. The grid refinement model of this reservoir model is shown in Fig. 6b.

The oil price is 377 \$/m^3. The treatment cost of the injected and produced water is 31 \$/m^3 with an annual discount rate of 0.1. The optimized parameters are the BHP with the upper bound of 3596.93 and 3596.93 psi, and the lower bound of 725.18 and 145.03 psi for injection and production wells, respectively. The key parameters of the StoSAG algorithm are set as follows. The perturbation ensemble size is 5 and the perturbation step is 0.01; the initial step size is 1.0 and the maximum number of step size cut is 5; the initial search position is the middle of the upper and lower limits of the well control, and the maximum number of iterations is 50.

First, we perform production optimization based on the StoSAG for the grid refinement model and EDFM model of the fractured reservoir shown in Fig. 6, respectively, and the optimization curves are shown in Fig. 7.

We can see that the optimization curves of both models are almost the same, but the NPV of the grid refinement model is

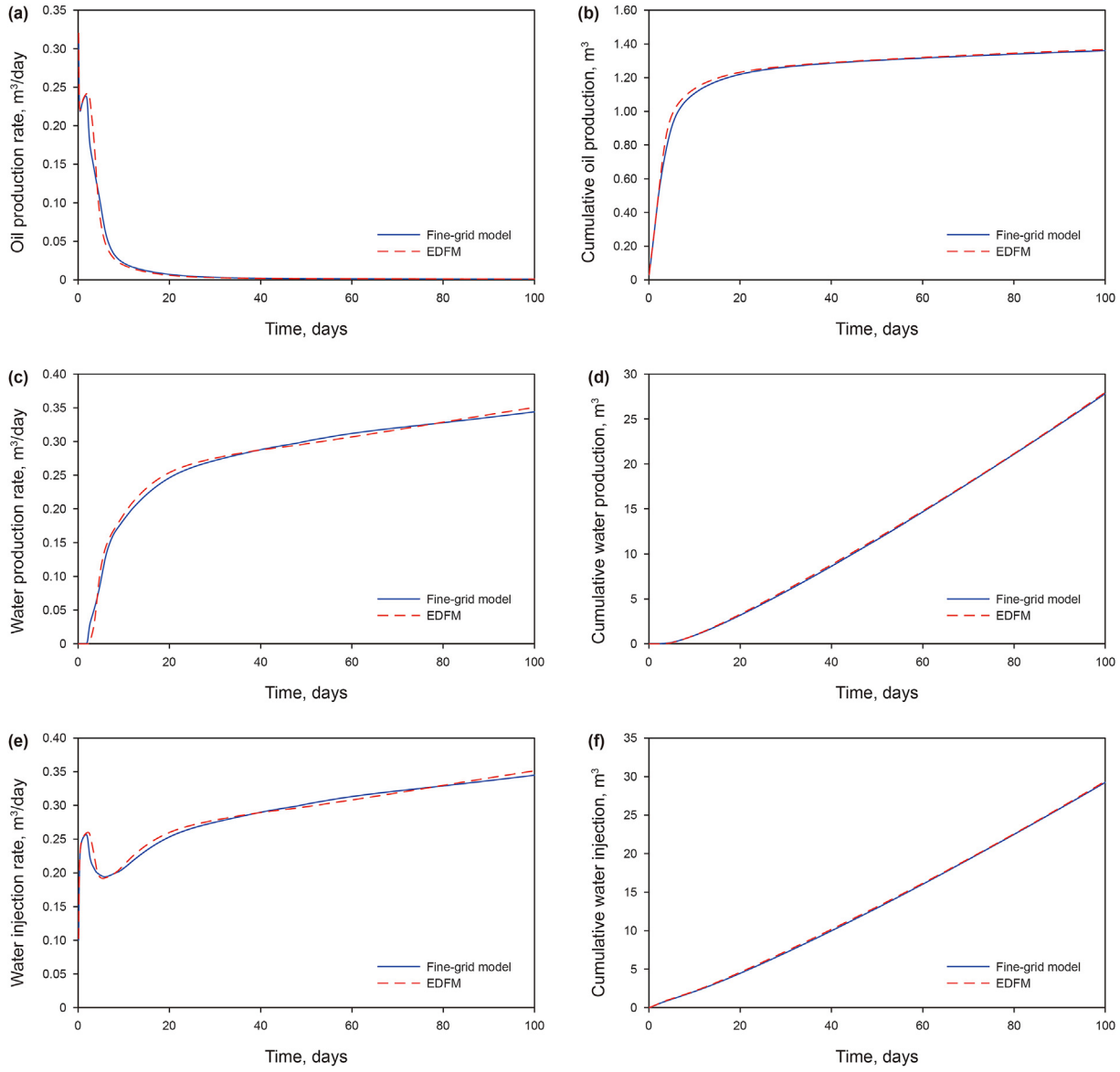

Fig. 5. Comparison of (**a**) oil production rate, (**b**) cumulative oil production, (**c**) water production rate, (**d**) cumulative water production, (**e**) water injection rate, and (**f**) cumulative water injection during 100 days for the model shown in Fig. 4, modeled by the Cartesian single porosity model and EDFM.

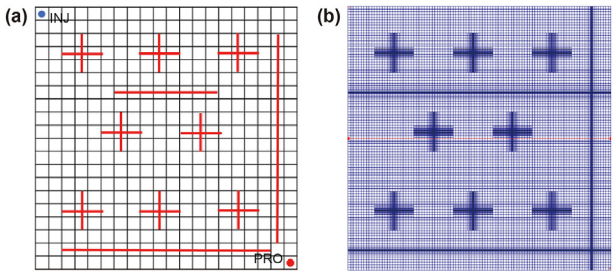

Fig. 6. (**a**) Fracture distribution and well location distribution of the conceptual model. (**b**) Grid refinement model.

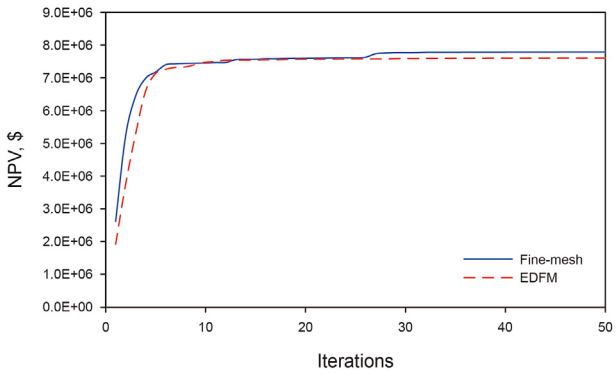

Fig. 7. Optimization curves of fine-mesh model and EDFM model based on StoSAG algorithm.

slightly higher than that of the EDFM model at the later stage of optimization. For this, we mainly consider that it is due to the influence of the stochastic nature of the StoSAG algorithm itself. It is

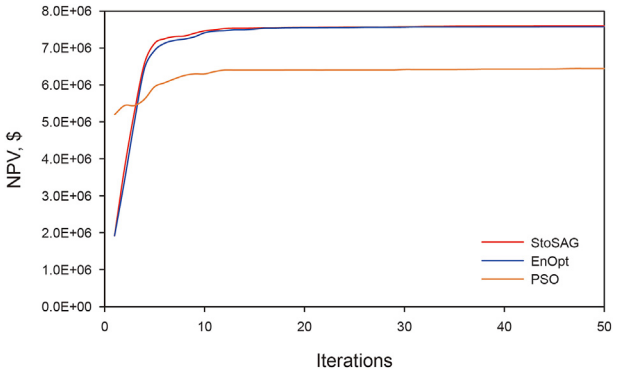

Fig. 8. Optimization curves of three optimization algorithms for production optimization of the reservoir model based on EDFM method.

Table 1
Optimization time of three optimization algorithms for this reservoir model based on EDFM method.

Algorithms	PSO	EnOpt	StoSAG
Optimization time, s	69447.98	11654.00	7699.22

worth noting the large difference in optimization times for both models using the same optimization parameters. The optimization times for the mesh refinement model and the EDFM model are 42,624.91 and 7699.22 s, respectively. The former takes 5.5 times longer than the latter. This reflects the great advantages of the EDFM model in production optimization.

Subsequently, in order to verify the adaptability of the StoSAG for production optimization in fractured reservoirs. We used the PSO, the EnOpt, and the StoSAG algorithm to optimize the production of the EDFM model of the above reservoir model under the same BHP constraint, respectively. The PSO algorithm parameters are set as follows. The inertia weight w is 0.8, the acceleration constants c_1 and c_2 are both 1.5, the particle population size is 100, and the maximum number of iterations is 50. The key parameter settings of the EnOpt are the same as those of the StoSAG. The optimization curves of three optimization algorithms for production optimization of the reservoir model based on EDFM are given in Fig. 8.

Combining the optimization curves of the three algorithms for the EDFM method for this reservoir model given in Fig. 8 and the optimization elapsed time given in Table 1, the PSO algorithm obtains the lowest final NPV compared to the other algorithms and takes the longest time. This also illustrates the limitations of derivative-free optimization algorithms such as the PSO algorithm, which rely on many reservoirs' simulation runs for the application of large reservoir optimization. The optimization curves of two approximate gradient algorithms are almost identical, which is because StoSAG is an improved EnOpt for robust optimization aspects, so the advantage is not obvious in the optimization results of a single deterministic reservoir. In this case, StoSAG algorithm takes shorter time and the efficiency of optimization is slightly higher than EnOpt.

From the final remaining oil distribution corresponding to the optimal well control obtained by the different algorithms given in Fig. 9, we can see that the three results have similar patterns of remaining oil distribution and are all concentrated at the edge of the reservoir. This is mainly due to the influence of two long fractures near the producing wells, which reduces the ripple effect of the injected water and forms a dead oil zone. On the other hand, the PSO algorithm obtained a slightly larger remaining oil distribution area than the other two algorithms, which is also reflected in the NPV curve in Fig. 8. This indicates that an effective optimization method can reduce the impact of fractures in the reservoir on the development economics to some extent.

6.2. Example 2: Egg model

The second case is based on the Egg model that has been widely used in the literature for well location and well control optimization. We introduce natural fractures to the geological realization of the Egg model. The Egg model contains 60 × 60 × 7 grid blocks, of which 18,553 grid blocks are active. The grid size is 8 m × 8 m × 4 m. The porosity of the substrate grid block is 0.2. The specific settings of geological and fluid parameters for the Egg model are described in Jansen et al. (2014). Eight injection wells and four production wells were placed in the model.

To consider the effect of fractures, we introduced 420 fracture meshes in the model with 14 fractures on seven layers of the model. The conductivity of all fractures is 8.3333×10^4 mD m. The horizontal permeability field and fracture distribution for each layer of the reservoir model are given in Fig. 10. The white line segments in the figure indicate fracture areas, the red solid dots denote production wells, and the blue solid dots denote injection wells. The initial formation pressure is 5801.51 psi. All production and injection wells are BHP controlled. The optimized parameters are the BHP of the wells, where the upper and lower limits are 5801.51 and 1450.37 psi for production wells and 8702.26 and 5801.51 psi for injection wells, respectively. The reservoir production life is set to 1500 days, during which a total of 30 control steps are set. The economic parameters and algorithm parameter settings involved in the optimization are the same as in Example 1, except that the number of particles is increased to 120 in the PSO.

The optimization curves for the three optimization algorithms

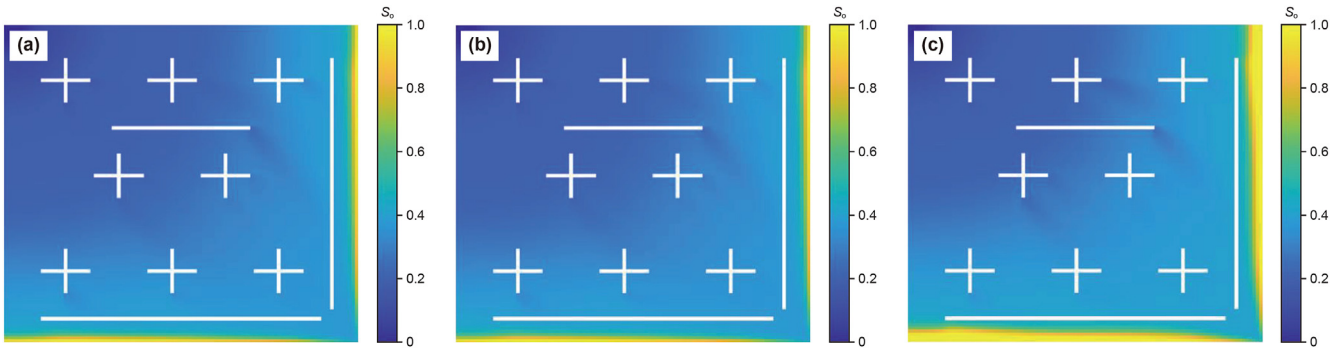

Fig. 9. Final remaining oil saturation field corresponding to the optimal production strategy obtained by (**a**) StoSAG, (**b**) EnOpt, and (**c**) PSO for Example 1.

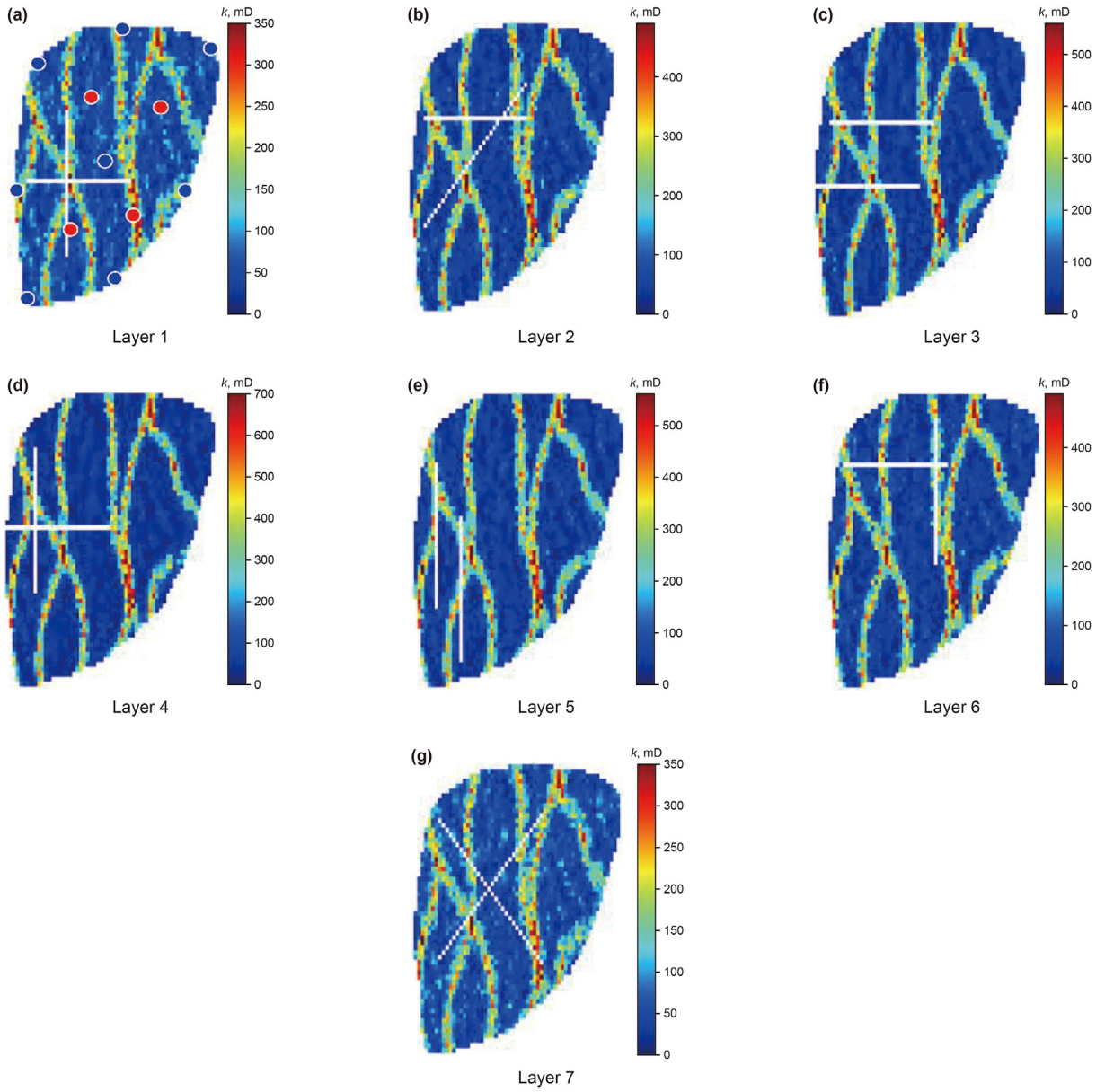

Fig. 10. Horizontal permeability field and fracture distribution in each layer of the reservoir.

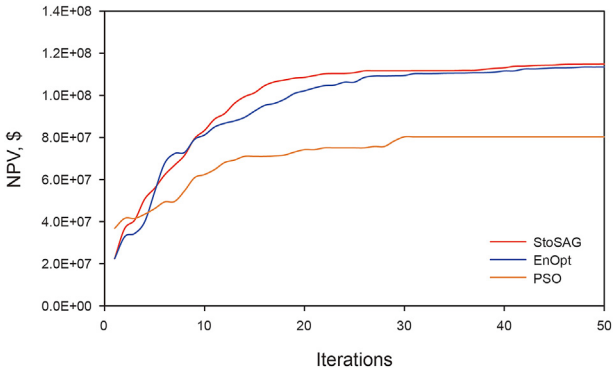

Fig. 11. Optimization curves of three optimization algorithms for production optimization of Egg model.

Table 2
Optimization time of three optimization algorithms for Egg model based on EDFM method.

Algorithms	PSO	EnOpt	StoSAG
Optimization time, s	714200.92	116199.22	154758.08

for the Egg model are given in Fig. 11, and the corresponding optimization times for the three algorithms are given in Table 2. It is clear that the computational efficiency of the other two algorithms is much higher than that of the PSO algorithm.

It is clear in Fig. 11 that the two approximate gradient algorithms have a better search capability and the PSO algorithm does not achieve the search results we expected. This may be due to the insufficient number of particles, but further increasing the number of particles will lead to more computational cost. For both approximate gradient algorithms, the final NPVs obtained are very

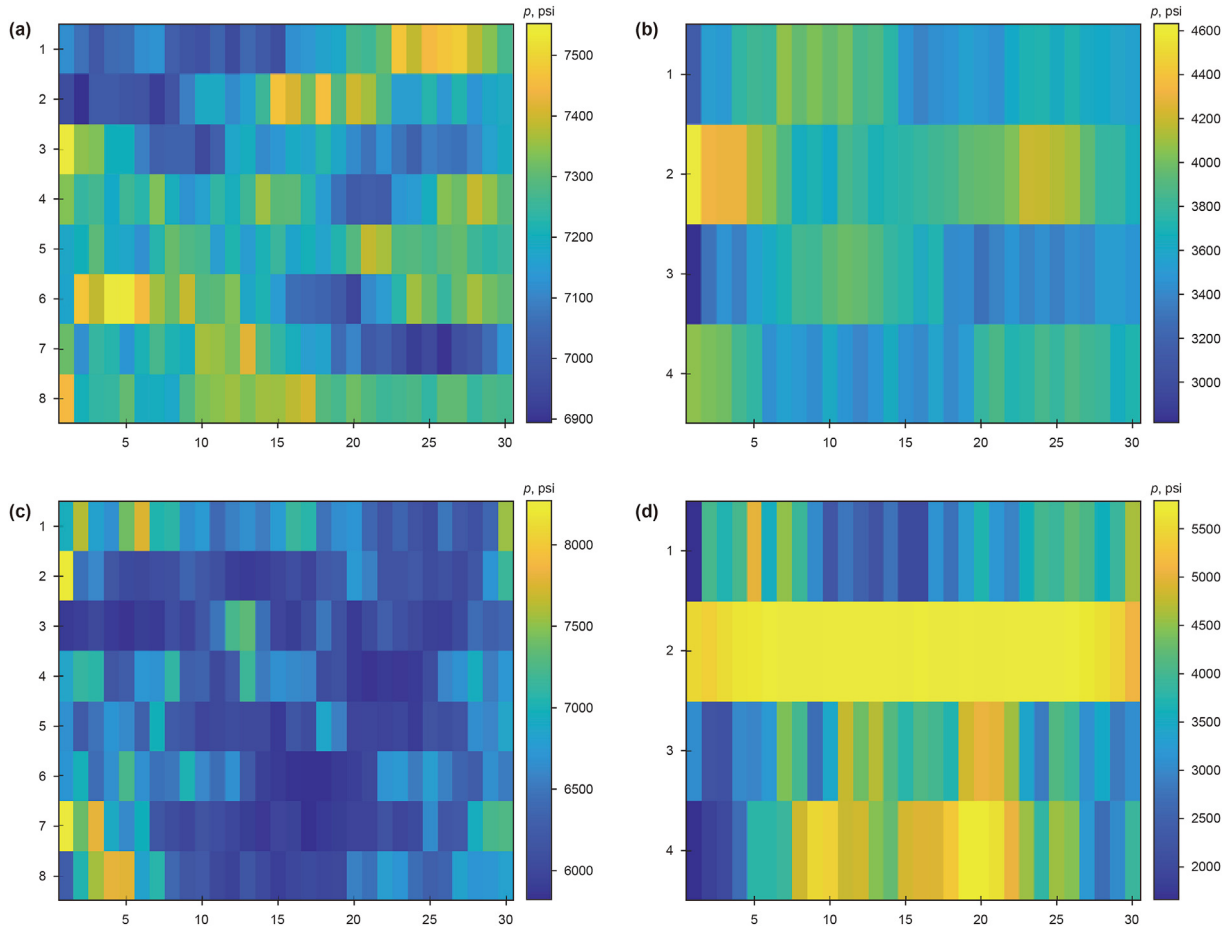

Fig. 12. BHP control of wells in the Egg model (**a**, **b**) before and (**c**, **d**) after optimization based on StoSAG (*left*: BHP control of injection wells; *right*: BHP control of production wells).

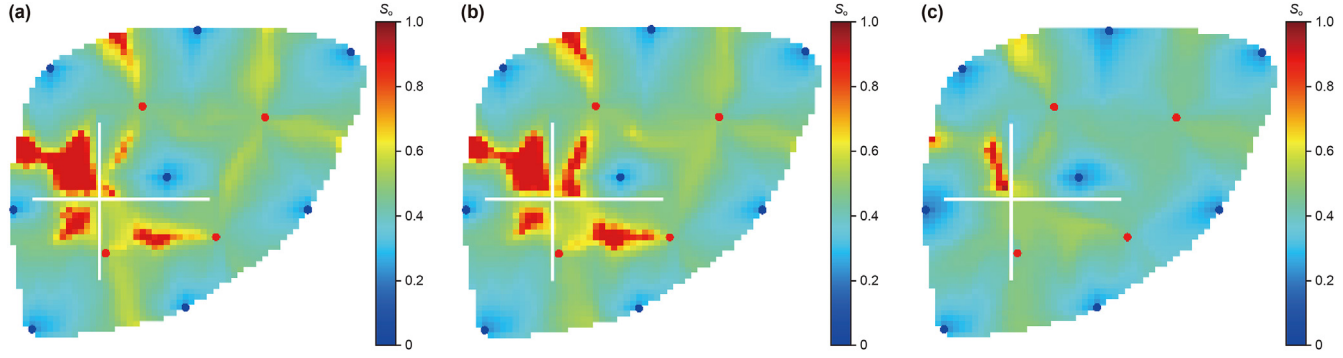

Fig. 13. Remaining oil saturation distribution for different approaches, Example 2, Layer 1. (**a**) StoSAG; (**b**) EnOpt; (**c**) PSO.

close and EnOpt is less than StoSAG in terms of optimization time. For StoSAG, more dichotomous search in subsequent iterations of the optimization process results in an increase in computation time. Therefore, in the subsequent practical applications, the introduction of dichotomous search with variable step size in the StoSAG algorithm may further improve the computational efficiency of the algorithm.

The BHP control of production and injection wells before and after optimization based on the StoSAG algorithm is presented in Fig. 12. We can see the most significant change in BHP control in production well 2, which is closest to the fracture. The optimized production of well 2 is operated at the highest BHP throughout the production process to avoid the occurrence of the early breakthrough of the injected water due to the presence of fractures and to improve the sweep efficiency of the injected water. For injection wells, the optimized injection well BHP control also showed a significant decrease compared to the pre-optimized BHP control.

The remaining oil distribution in layer 1 corresponding to the best well control obtained by the three algorithms is given in Fig. 13, and we can see that the dead oil zone is mainly concentrated in the area between the fractures. The results of residual oil distribution are significantly different from Case 1. The remaining oil distribution corresponding to StoSAG and EnOpt, which obtained better optimization results in Fig. 11, is much larger than that of the

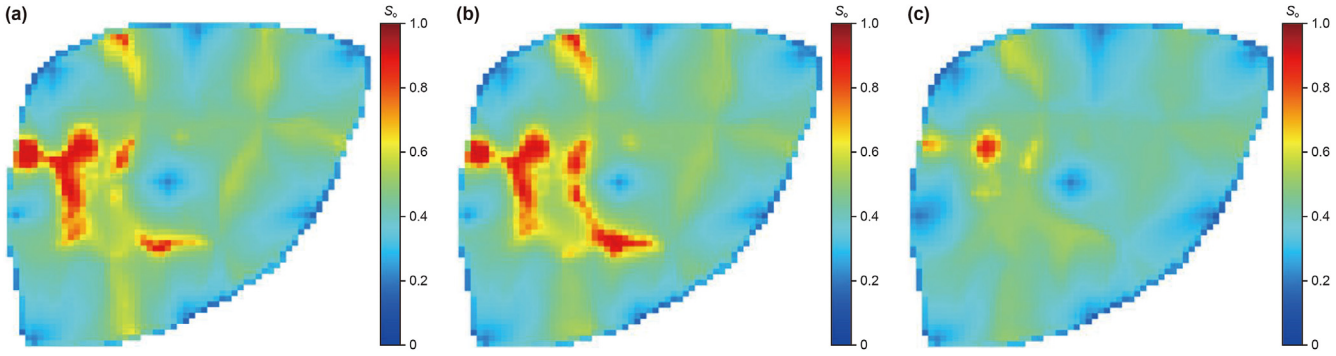

Fig. 14. Average remaining oil saturation distribution for different approaches, Example 2. (**a**) StoSAG; (**b**) EnOpt; (**c**) PSO.

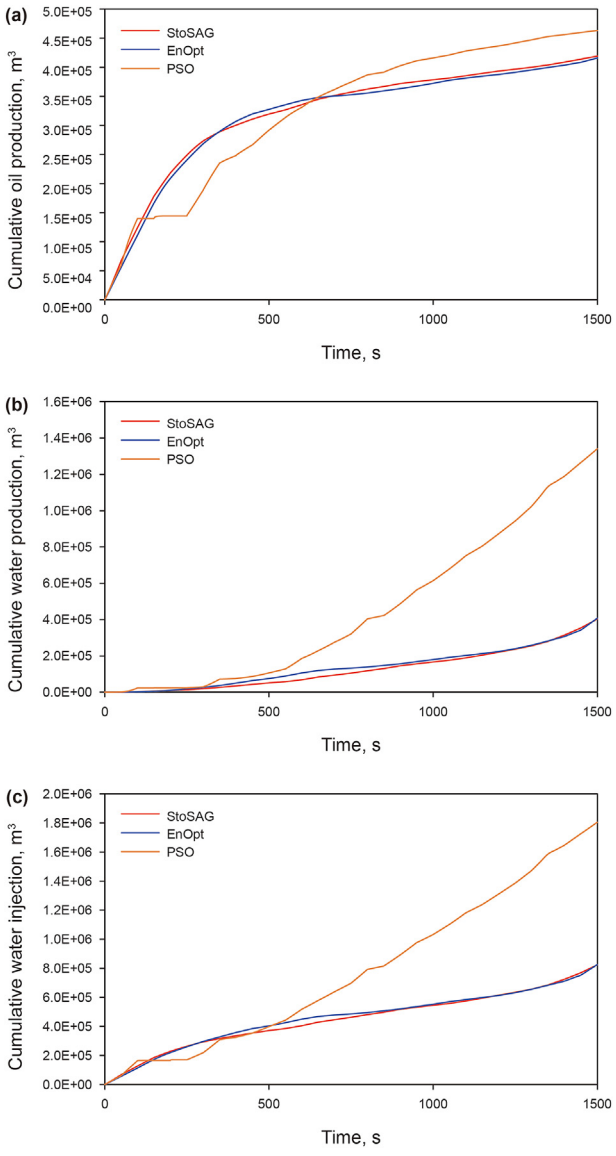

Fig. 15. Comparison of three optimization algorithms for (**a**) cumulative oil production, (**b**) cumulative water production, and (**c**) cumulative water injection, Example 2.

PSO algorithm. Considering the inter-layer differences of the Egg model, the results of layer 1 are not generalized. Therefore, we further present in Fig. 14 the reservoir average remaining oil distribution corresponding to the best well control obtained by the three algorithms. That is the arithmetic average of the remaining oil in each layer for the effective grid at the same location in the reservoir. The average remaining oil distribution of the PSO algorithm in Fig. 14 is still much smaller than the other two algorithms. This is also confirmed in the cumulative oil production curve in Fig. 15a.

The cumulative water production curve in Fig. 15b and the cumulative injection water curve in Fig. 15c also give explanations for these differences. The higher recovery of PSO is achieved at the cost of high injection and high-water production. The presence of fractures in the reservoir affects the injection water drive efficiency to a large extent and reduces the injection efficiency ratio. Therefore, although it is higher than the other two algorithms in terms of recovery rate, the high cost of injection water and treatment cost of produced water makes the final economic benefit much smaller than the other two algorithms.

6.3. Example 3: PUNQ-S3 model

Considering that the gas phase in the formation fluid is more sensitive to the existence of fractures, and the former two cases are oil-water two-phase reservoir models, we add an oil-gas-water three-phase reservoir model at the end. This model is based on the PUNQ-S3 reservoir model and is realized by embedding two fractures in each layer of the reservoir. Like the Egg model, the PUNQ-S3 model is based on actual reservoirs and is widely used in numerical simulation and development optimization of reservoirs. The model contains 19 × 28 × 5 grid blocks, of which 1761 blocks are active.

To consider the effect of fractures, we introduced 100 fracture meshes in the model with 10 fractures on five layers of the model. The conductivity of all fractures is 8.3333×10^4 mD m. The permeability and fracture distribution of each layer are shown in Fig. 16. Also due to the strength of the aquifer, there are only six vertical production wells in the original development program, which do not require water injection wells for pressure retention. Therefore, here we only optimize production for these six production wells. All production wells are BHP controlled. The optimized parameters are the BHP of the wells, where the upper and lower limits are 2900.75 and 725.19 psi for these production wells. The economic and algorithmic parameters involved in the optimization process are the same as in Case 2, except that the yield of the output gas needs to be additionally considered. Here we set the price of output gas to 0.007 \$/m^3 (Liu and Reynolds, 2021). The optimization curves of each of the three optimization algorithms for production optimization of fractured reservoirs based on the PUNQ-S3 model are given in Fig. 17, and the corresponding

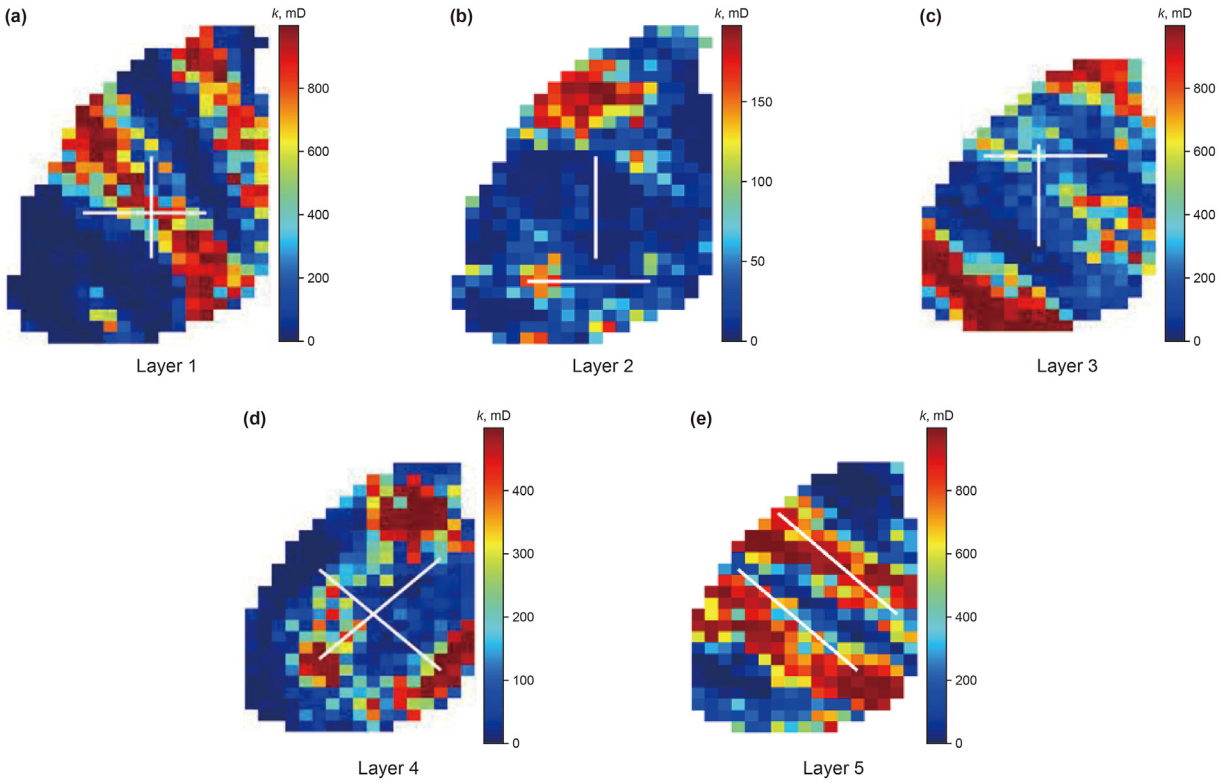

Fig. 16. Permeability and fracture distribution of each layer, Example 3.

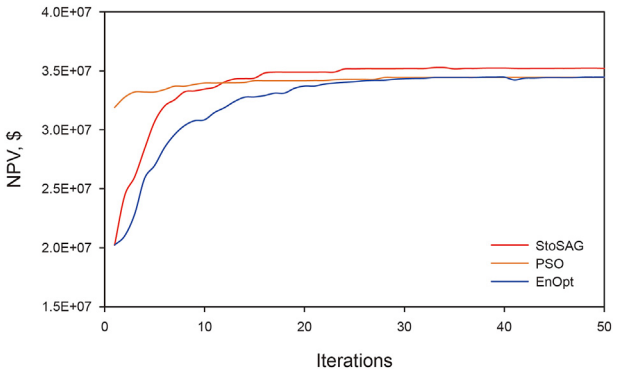

Fig. 17. Optimization curves for three optimization algorithms for Example 3.

Table 3
Optimization time of three optimization algorithms for PUNQ-S3 model based on EDFM method.

Algorithms	PSO	EnOpt	StoSAG
Optimization time, s	42388.24	41851.55	62221.65

algorithmic time consumptions are listed in Table 3.

As can be seen in Fig. 17, the StoSAG algorithm obtains the highest final NPV, but the difference with the result obtained by the EnOpt algorithm is not significant. The PSO algorithm performs the same as in the previous two cases, still achieving the worst final NPV. It should be noted that the computational time consumed by each algorithm given in Table 3 is the same as in Case 2, due to the large computational effort of PSO. Therefore, we use a parallel version of the PSO algorithm and call 6 cores to accelerate the computation, so the time cost disadvantage of the PSO algorithm is not obvious in the final computation elapsed time. Instead, the computation time of StoSAG is the longest.

The final remaining oil distribution of the PUNQ-S3 model obtained by the three algorithms is presented in Fig. 18. The remaining oil distribution of the three algorithms has similar areas of remaining oil concentration and high residual oil saturation. This is mainly because the need for injection is not considered in the initial model and only production wells are available. Due to the presence of fractures in the reservoir and the proximity of some of the fractures to the producing wells. This leads to a large portion of the crude oil in the reservoir being difficult to move.

The cumulative oil production, cumulative water production, and cumulative gas production corresponding to the three algorithms are given in Fig. 19. We can see that all the cumulative production curves reach the inflection point earlier compared to the production life of 3000 days. And generally, the development optimization based on the PUNQ-S3 model is chosen for a longer period, for example, 20 years (Ding et al., 2020). This indicates that the presence of fractures can greatly accelerate the development rate of the reservoir. Therefore, in further studies, production optimization for fractured reservoirs needs to consider the cost of the daily operation of the wells to avoid long-time ineffective operation. This is because, in practice, the daily operation of wells also requires costs.

7. Conclusions

In the work, we first verified the effectiveness of the EDFM method by comparison with the grid refinement model for different types of fracture distribution in the reservoir. Then, we perform StoSAG-based optimization of the grid refinement model and EDFM model for the same fractured reservoir separately with

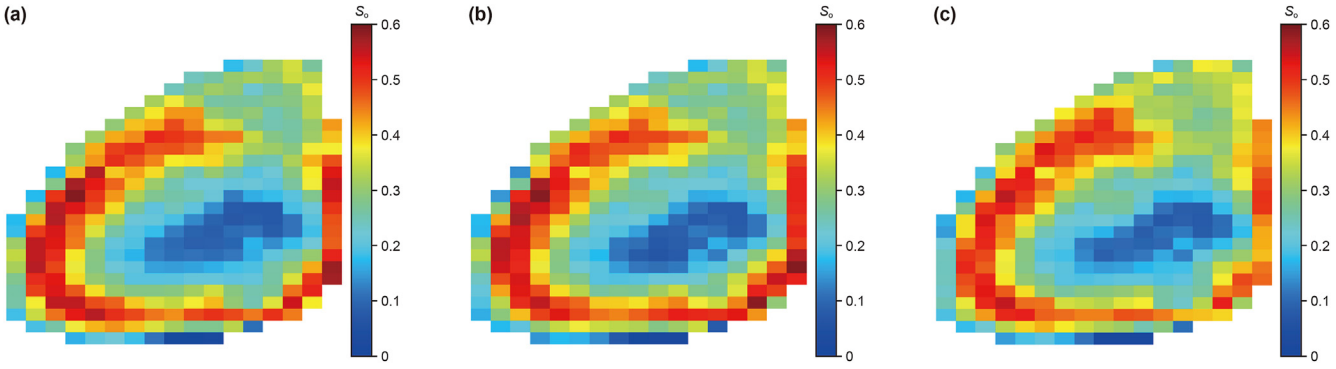

Fig. 18. Average remaining oil saturation distribution for different approaches, Example 3. (**a**) StoSAG; (**b**) EnOpt; (**c**) PSO.

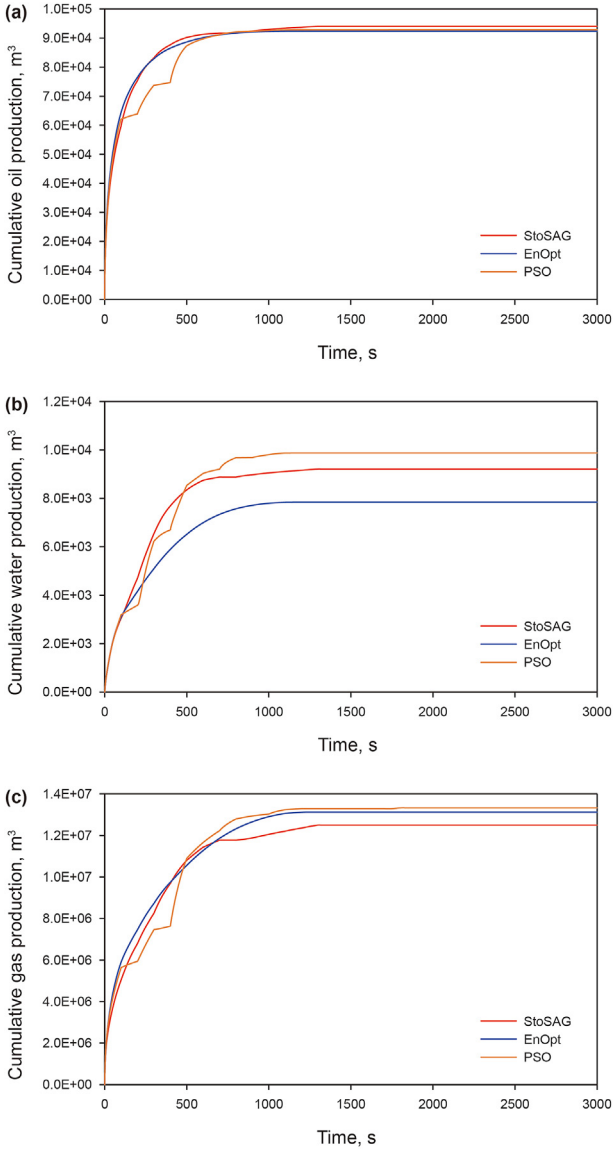

Fig. 19. Comparison of three optimization algorithms for (**a**) cumulative oil production, (**b**) cumulative water production, and (**c**) cumulative gas production, Example 3.

NPV as the objective function. We further validated the effectiveness of the couple of EDFM and StoSAG algorithms. Finally, we apply the StoSAG, EnOpt, and PSO algorithms to conceptual models of a single deterministic fractured reservoir and well control optimization of two actual reservoir models with the introduction of fractures, respectively. Compared with the initial guessed well control of the three models, the optimized well control of all three optimization algorithms obtained a large improvement in NPV, among which the optimization effect of StoSAG and EnOpt algorithms was the most significant. The disadvantage of PSO is obvious in terms of computational efficiency. Combining the performance of the three algorithms in this paper in the case of deterministic optimization of fractured reservoir production, StoSAG and EnOpt algorithms achieved the best optimization results. However, in terms of optimization time consumption, both are limited by the built-in fastest ascent method, and the computational efficiency varies in different cases. The optimization results also show that the presence of fractures has a huge impact on the injection water sweep efficiency. The use of reasonable optimization algorithms can attenuate the adverse effects of fractures on reservoir development and improve the economic benefits of reservoir development.

Declaration of competing interest

The authors declare that they have no known competing financial interests or personal relationships that could have appeared to influence the work reported in this paper.

Acknowledgement

This study was supported by the National Natural Science Foundation of China (51904323, 52174052).

References

Al Dossary, M.A., Nasrabadi, H., 2016. Well placement optimization using imperialist competitive algorithm. J. Petrol. Sci. Eng. 147, 237–248. https://doi.org/10.1016/j.petrol.2016.06.017.

Chai, Z., Yan, B., Killough, J.E., Wang, Y., 2018a. An efficient method for fractured shale reservoir history matching: the embedded discrete fracture multi-continuum approach. J. Petrol. Sci. Eng. 160, 170–181. https://doi.org/10.1016/j.petrol.2017.10.055.

Chai, Z., Tang, H., He, Y., Killough, J., Wang, Y., 2018b. Uncertainty quantification of the fracture network with a novel fractured reservoir forward model. In: SPE Annual Technical Conference and Exhibition. https://doi.org/10.2118/191395-MS.

Chang, C., Liu, C., Li, Y., Li, X., Yu, W., Miao, J., Sepehrnoori, K., 2020. A novel optimization workflow coupling statistics-based methods to determine optimal well spacing and economics in shale gas reservoir with complex natural fractures. Energies 13 (15), 3965. https://doi.org/10.3390/en13153965.

Chen, B., Reynolds, A.C., 2018. CO_2 water-alternating-gas injection for enhanced oil recovery: optimal well controls and half-cycle lengths. Comput. Chem. Eng. 113, 44–56. https://doi.org/10.1016/j.compchemeng.2018.03.006.

Chen, B., Fonseca, R.M., Leeuwenburgh, O., Reynolds, A.C., 2017. Minimizing the risk in the robust life-cycle production optimization using stochastic simplex

approximate gradient. J. Petrol. Sci. Eng. 153, 331–344. https://doi.org/10.1016/j.petrol.2017.04.001.
Chen, B., Xu, J., 2019. Stochastic simplex approximate gradient for robust life-cycle production optimization: applied to brugge field. J. Energ. Resour-ASME. 141 (9). https://doi.org/10.1115/1.4043244.
Chen, G., Zhang, K., Zhang, L., Xue, X., Ji, D., Yao, C., Yao, J., Yang, Y., 2020. Global and local surrogate-model-assisted differential evolution for waterflooding production optimization. SPE J. 25 (1), 105–118. https://doi.org/10.2118/199357-PA.
Ding, S., Lu, R., Xi, Y., Liu, G., Ma, J., 2020. Efficient well placement optimization coupling hybrid objective function with particle swarm optimization algorithm. Appl. Soft Comput. 95, 106511. https://doi.org/10.1016/j.asoc.2020.106511.
Feng, Q.H., Li, S.S., Zhang, X.M., Gao, X.F., Ni, J.H., 2022. Well production optimization using streamline features-based objective function and Bayesian adaptive direct search algorithm. Petrol. Sci. 19 (6), 2879–2894. https://doi.org/10.1016/j.petsci.2022.06.016.
Fiallos, M.X., Yu, W., Ganjdanesh, R., Kerr, E., Sepehrnoori, K., Miao, J., Ambrose, R., 2019. Modeling interwell interference due to complex fracture hits in eagle ford using EDFM. In: International Petroleum Technology Conference. https://doi.org/10.2523/IPTC-19468-MS.
Fonseca, R.R.M., Chen, B., Jansen, J.D., Reynolds, A., 2017. A stochastic simplex approximate gradient (StoSAG) for optimization under uncertainty. Int. J. Numer. Methods Eng. 109 (13), 1756–1776. https://doi.org/10.1002/nme.5342.
Hajibeygi, H., Karvounis, D., Jenny, P., 2011. A hierarchical fracture model for the iterative multiscale finite volume method. J. Comput. Phys. 230 (24), 8729–8743. https://doi.org/10.1016/j.jcp.2011.08.021.
Han, X., Zhong, L., Wang, X., Liu, Y., Wang, H., 2021. Well placement and control optimization of horizontal steamflooding wells using derivative-free algorithms. SPE Reservoir Eval. Eng. 24 (1), 174–193. https://doi.org/10.2118/203821-PA.
Jansen, J.D., Fonseca, R.M., Kahrobaei, S., Siraj, M.M., Van Essen, G.M., van den Hof, P.M.J., 2014. The egg model–a geological ensemble for reservoir simulation. Geosci. Data. J. 1 (2), 192–195. https://doi.org/10.1002/gdj3.21.
Jia, B., Xian, C.G., 2022. Permeability measurement of the fracture-matrix system with 3D embedded discrete fracture model. Petrol. Sci. 19 (4), 1757–1765. https://doi.org/10.1016/j.petsci.2022.01.010.
Jia, D., Liu, H., Zhang, J., Gong, B., Pei, X., Wang, Q., Yang, Q., 2020. Data-driven optimization for fine water injection in a mature oil field. Petrol. Explor. Dev. 47 (3), 674–682. https://doi.org/10.1016/S1876-3804(20)60084-2.
Karimi-Fard, M., Firoozabadi, A., 2003. Numerical simulation of water injection in fractured media using the discrete-fracture model and the Galerkin method. SPE Reservoir Eval. Eng. 6 (2), 117–126. https://doi.org/10.2118/83633-PA.
Karimi-Fard, M., Durlofsky, L.J., Aziz, K., 2004. An efficient discrete-fracture model applicable for general-purpose reservoir simulators. SPE J. 9 (2), 227–236. https://doi.org/10.2118/88812-PA.
Lee, S., Stephen, K., 2019. Field application study on automatic history matching using particle swarm optimization. In: SPE Reservoir Characterisation and Simulation Conference and Exhibition. https://doi.org/10.2118/196678-MS.
Li, L., Lee, S.H., 2008. Efficient field-scale simulation of black oil in a naturally fractured reservoir through discrete fracture networks and homogenized media. SPE Reservoir Eval. Eng. 11 (4), 750–758. https://doi.org/10.2118/103901-PA.
Liu, Z., Forouzanfar, F., 2018. Ensemble clustering for efficient robust optimization of naturally fractured reservoirs. Comput. Geosci. 22, 283–296. https://doi.org/10.1007/s10596-017-9689-1.
Liu, Z., Reynolds, A.C., 2021. Gradient-enhanced support vector regression for robust life-cycle production optimization with nonlinear-state constraints. SPE J. 26 (4), 1590–1613. https://doi.org/10.2118/204236-PA.
Liu, H., Rao, X., Xiong, H., 2020. Evaluation of CO_2 sequestration capacity in complex-boundary-shape shale gas reservoirs using projection-based embedded discrete fracture model (pEDFM). Fuel 277, 118201. https://doi.org/10.1016/j.fuel.2020.118201.
Lorentzen, R.J., Berg, A., Naevdal, G., Vefring, E.H., 2006. A new approach for dynamic optimization of water flooding problems. In: Intelligent Energy Conference and Exhibition. https://doi.org/10.2118/99690-MS.
Lu, R., Forouzanfar, F., Reynolds, A.C., 2017. An efficient adaptive algorithm for robust control optimization using StoSAG. J. Petrol. Sci. Eng. 159, 314–330. https://doi.org/10.1016/j.petrol.2017.09.002.
Ma, Z., Volkov, O., Durlofsky, L.J., 2022. Multigroup strategy for well control optimization. J. Petrol. Sci. Eng. 214, 110448. https://doi.org/10.1016/j.petrol.2022.110448.
Moinfar, A., Varavei, A., Sepehrnoori, K., Johns, R.T., 2014. Development of an efficient embedded discrete fracture model for 3D compositional reservoir simulation in fractured reservoirs. SPE J. 19 (2), 289–303. https://doi.org/10.2118/154246-PA.
Murray, R.L., Hopkins, R.S., Valentine, D.K., 2020. Network optimization models at greater Kuparuk area using neural networks and genetic algorithms. In: SPE Annual Technical Conference and Exhibition. https://doi.org/10.2118/201760-MS.
Nasir, Y., Volkov, O., Durlofsky, L.J., 2022. A two-stage optimization strategy for large-scale oil field development. Optim. Eng. 23, 361–395. https://doi.org/10.1007/s11081-020-09591-y.
Nwaozo, J.E., 2006. Dynamic Optimization of a Water Flood Reservoir. Doctoral Dissertation. University of Oklahoma.
Olorode, O., Wang, B., Rashid, H.U., 2020. Three-dimensional projection-based embedded discrete-fracture model for compositional simulation of fractured reservoirs. SPE J. 25 (4), 2143–2161. https://doi.org/10.2118/201243-PA.
Pan, S.Y., Liao, Q., Liang, Y.T., 2022. Multivariable sales prediction for filling stations via GA improved BiLSTM. Petrol. Sci. 19 (5), 2483–2496. https://doi.org/10.1016/j.petsci.2022.05.005.
Rao, X., Cheng, L., Cao, R., Jia, P., Liu, H., Du, X., 2020. A modified projection-based embedded discrete fracture model (pEDFM) for practical and accurate numerical simulation of fractured reservoir. J. Petrol. Sci. Eng. 187, 106852. https://doi.org/10.1016/j.petrol.2019.106852.
Rao, X., Xin, L., He, Y., Fang, X., Gong, R., Wang, F., Zhao, H., Shi, J., Xu, Y., Dai, W., 2022. Numerical simulation of two-phase heat and mass transfer in fractured reservoirs based on projection-based embedded discrete fracture model (pEDFM). J. Petrol. Sci. Eng. 208, 109323. https://doi.org/10.1016/j.petrol.2021.109323.
Soleimani, M., 2017. Naturally fractured hydrocarbon reservoir simulation by elastic fracture modeling. Petrol. Sci. 14 (2), 286–301. https://doi.org/10.1007/s12182-017-0162-5.
Sun, Q., Xu, J., 2022. Investigation of fluid flow mechanisms in fractured porous media using a Laplace transformation coupled embedded discrete fracture protocol. J. Petrol. Sci. Eng. 208, 109356. https://doi.org/10.1016/j.petrol.2021.109356.
Ţene, M., Bosma, S.B., Al Kobaisi, M.S., Hajibeygi, H., 2017. Projection-based embedded discrete fracture model (pEDFM). Adv. Water Resour. 105, 205–216. https://doi.org/10.1016/j.advwatres. 2017.05.009.
Torcuk, M.A., Kurtoglu, B., Alharthy, N., Kazemi, H., 2013. Analytical solutions for multiple matrix in fractured reservoirs: application to conventional and unconventional reservoirs. SPE J. 18 (5), 969–981. https://doi.org/10.2118/164528-PA.
Torres, M.F., Morales, A., Yu, W., Miao, J., 2021. Characterization of complex hydraulic fractures in Eagle Ford shale oil development through embedded discrete fracture modeling. Petrol. Explor. Dev. 48 (3), 713–720. https://doi.org/10.1016/S1876-3804(21)60057-5.
Tukur, A.D., Nzerem, P., Nsan, N., Okafor, I.S., Gimba, A., Ogolo, O., Oluwaseun, A., Andrew, O., 2019. Well placement optimization using simulated annealing and genetic algorithm. In: SPE Nigeria Annual International Conference and Exhibition. https://doi.org/10.2118/198858-MS.
Warren, J.E., Root, P.J., 1963. The behavior of naturally fractured reservoirs. SPE J. 3 (3), 245–255. https://doi.org/10.2118/426-PA.
Wang, X., Haynes, R.D., Feng, Q., 2016. A multilevel coordinate search algorithm for well placement, control and joint optimization. Comput. Chem. Eng. 95, 75–96. https://doi.org/10.1016/j.compchemeng.2016.09.006.
Wu, Y., Cui, Z.Y., Lin, H., Wang, Y.F., Feng, X., 2022. An optimization method for shale gas gathering system-Consideration of reliability enhancement under earthquake-related uncertainties. Petrol. Sci. 19 (5), 2431–2447. https://doi.org/10.1016/j.petsci.2021.12.029.
Xu, Y., Yu, W., Li, N., Lolon, E., Sepehrnoori, K., 2018. Modeling well performance in Piceance Basin Niobrara formation using embedded discrete fracture model. In: Unconventional Resources Technology Conference. https://doi.org/10.15530/urtec-2018-2901327.
Xu, Y., Sepehrnoori, K., 2019. Development of an embedded discrete fracture model for field-scale reservoir simulation with complex corner-point grids. SPE J. 24 (4), 1552–1575. https://doi.org/10.2118/195572-PA.
Xue, L., Gu, S.H., Jiang, X.E., Liu, Y.T., Yang, C., 2021. Ensemble-based optimization of hydraulically fractured horizontal well placement in shale gas reservoir through Hough transform parameterization. Petrol. Sci. 18, 839–851. https://doi.org/10.1007/s12182-021-00560-3.
Yang, H., Kim, J., Choe, J., 2017. Field development optimization in mature oil reservoirs using a hybrid algorithm. J. Petrol. Sci. Eng. 156, 41–50. https://doi.org/10.1016/j.petrol. 2017.05.009.
Zhang, K., Zhang, L., Yao, J., Chen, Y., Lu, R., 2014. Water flooding optimization with adjoint model under control constraints. J. Hydrodyn. Ser. B 26 (1), 75–85. https://doi.org/10.1016/S1001-6058(14)60009-3.
Zhu, D., Hu, Y., Cui, M., Chen, Y., Liang, C., Cai, W., He, Y., Wang, X., Chen, H., Li, X., 2020. Productivity simulation of hydraulically fractured wells based on hybrid local grid refinement and embedded discrete fracture model. Petrol. Explor. Dev. 47 (2), 365–373. https://doi.org/10.1016/S1876-3804(20)60053-2.
Zhu, Q., Lin, B., Yang, G., Wang, L., Chen, M., 2022. Intelligent production optimization method for a low pressure and low productivity shale gas well. Petrol. Explor. Dev. 49 (4), 886–894. https://doi.org/10.11698/PED.20210781.